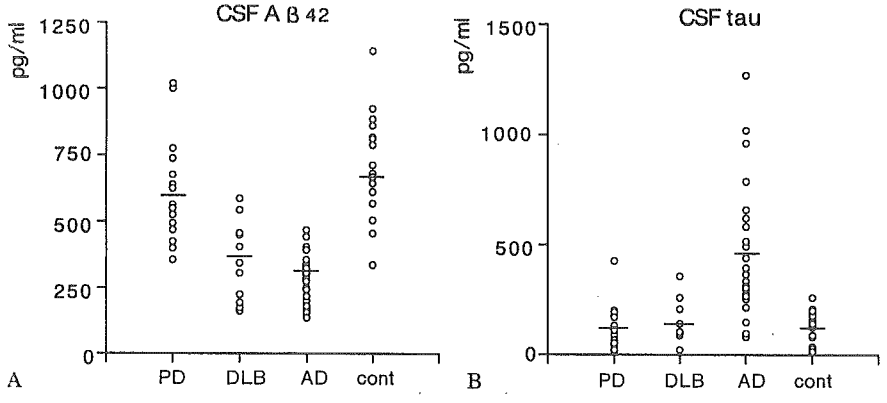

Figure. (A, B) The levels of CSF amyloid β42 (Aβ42; A) and tau (B) in patients with PD, dementia with Lewy bodies (DLB), or AD, and in control subjects (cont). Horizontal bars represent the mean value of each group.

Key words: Dementia with Lewy bodies—CSF—Amyloid β42—Tau.

From the Department of Neurology, Tokyo Metropolitan Geriatric Hospital, Japan.

Received September 22, 1999. Accepted in final form January 12, 2000.

Address correspondence and reprints to Dr. Kazutomi Kanemaru, Department of Neurology, Tokyo Metropolitan Geriatric Hospital, 35-2 Sakae, cho, Itabashi, ku, Tokyo 173-0015, Japan; e-mail: kazukane@tmig.or.jp

Copyright © 2000 by the American Academy of Neurology

References

1. McKeith IG, Galasko D, Kosaka K, et al. Consensus guidelines for the clinical and pathologic diagnosis of dementia with Lewy bodies (DLB): report of the Consortium on DLB International Workshop. Neurology 1996;47:1113–1124.
2. Hansen LA, Masliah E, Galasko D, Terry RD. Plaque-only Alzheimer disease is usually the Lewy body variant, and vice versa. J Neuropathol Exp Neurol 1993;52:648–654.
3. Harrington CR, Perry RH, Perry EK, et al. Senile dementia of Lewy body type and Alzheimer type are biochemically distinct in terms of paired helical filaments and hyperphosphorylated tau protein. Dementia 1994; 5:215–228.
4. Hulstaert F, Blennow K, Ivanoiu A, et al. Improved discrimination of AD patients using β-amyloid(1-42) and tau levels in CSF. Neurology 1999; 52:1555–1562.
5. McKhann G, Drachman D, Folstein M, et al. Clinical diagnosis of Alzheimer's disease: report of the NINCDS-ADRDA Work Group under the auspices of Department of Health and Human Services Task Force on Alzheimer's disease. Neurology 1984;34:939–944.
6. Arai H, Morikawa Y, Higuchi M, et al. Cerebrospinal fluid tau levels in neurodegenerative diseases with distinct tau-related pathology. Biochem Biophys Res Commun 1997;236:262–264.
7. Tapiola T, Overmyer M, Lehtovirta M, et al. The level of cerebrospinal fluid tau correlates with neurofibrillary tangles in Alzheimer's disease. Neuroreport 1997;8:3961–3963.

Acta Neurol Scand 2005: 112: 103–107 DOI: 10.1111/j.1600-0404.2005.00432.x

Copyright © Blackwell Munksgaard 2005

ACTA NEUROLOGICA SCANDINAVICA

Function of sigma$_1$ receptors in Parkinson's disease

Mishina M, Ishiwata K, Ishii K, Kitamura S, Kimura Y, Kawamura K, Oda K, Sasaki T, Sakayori O, Hamamoto M, Kobayashi S, Katayama Y. Function of sigma$_1$ receptors in Parkinson's disease.
Acta Neurol Scand 2005: 112: 103–107. © Blackwell Munksgaard 2005.

Objective – The objective of this study was to investigate the mapping of sigma$_1$ receptors in Parkinson's disease (PD) using [^{11}C]SA4503 and positron emission tomography (PET), and to assess whether sigma$_1$ receptors are involved in the damaged dopaminergic system in PD patients. *Materials and methods* – We studied seven normal volunteers and six PD patients. The low density of dopamine transporters and the normal or high density of dopamine receptors were confirmed in the putamen of all patients using [^{11}C]CFT and [^{11}C]RAC PET. A dynamic series of PET data acquisition was performed with arterial blood sampling. We computed the binding potential (BP) of [^{11}C]SA4503. *Results* – In PD patients, the BP was significantly lower on the more affected than the less affected side of the anterior putamen, although there was no significant difference with respect to the BP between patients and controls. *Conclusions* – Release of dopamine is reduced asymmetrically in the putamen of early PD. [^{11}C]SA4503 PET is an indicator of presynaptic dopaminergic damage in PD.

M. Mishina[1,2,3], K. Ishiwata[2], K. Ishii[2], S. Kitamura[3,4], Y. Kimura[2], K. Kawamura[2], K. Oda[2], T. Sasaki[2], O. Sakayori[3,5], M. Hamamoto[3,5], S. Kobayashi[6], Y. Katayama[3]

[1]The Department of Neurology, Neurological Institute, Nippon Medical School Chiba-Hokusoh Hospital, Inba-Gun, Chiba; [2]Positron Medical Center, Tokyo Metropolitan Institute of Gerontology, Itabashi-ku, Tokyo; [3]The Second Department of Internal Medicine, Nippon Medical School, Bunkyo-ku,Tokyo; [4]The Department of Internal Medicine, Nippon Medical School Second Hospital, Kawasaki-shi, Kanagawa; [5]The Department of Internal Medicine, Nippon Medical School Chiba-Hokusoh Hospital, Inba-gun, Chiba; [6]The Department of Neurosurgery, Neurological Institute, Nippon Medical School Chiba-Hokusoh Hospital, Inba-gun, Chiba, Japan

Key words: dopamine; Parkinson's disease; positron emission tomography; sigma$_1$ receptor

Masahiro Mishina, Neurological Institute, Nippon Medical School Chiba-Hokusoh Hospital, 1715 Kamagari, Inba-mura, Inba-gun Chiba 270-1694, Japan
Tel.: 81-476-99-1111
Fax: 81-476-99-1908
e-mail: mishina@nms.ac.jp

Accepted for publication April 1, 2005

Introduction

Parkinson's disease (PD) is a progressive degenerative neurological disorder characterized clinically by resting tremor, bradykinesia, cogwheel rigidity, and postural instability. These symptoms result primarily from the loss of dopaminergic neurons in the substantia nigra (1). Positron emission tomography (PET) can obtain *in vivo* images of dopamine metabolism in the patients with PD (2). A study with [^{18}F]dopa PET demonstrated that presynaptic dopaminergic function in the dorsal putamen is reduced to almost 50% of normal in the patients with early PD (3). Using PET with [^{11}C] [^{11}C]2β-carbomethoxy-3β-(4-fluorophenyl) tropane (CFT), the distribution of presynaptic membrane dopamine transporter (DAT) in the human brain can be shown (4). Uptake of DAT ligand PET is thought to be more sensitive to detect dopaminergic dysfunction in early PD than [^{18}F]dopa PET, because of compensatory down-regulation of DAT to maintain dopamine levels in the synapse (5, 6). Using PET with [^{11}C]raclopride, we can observe that the distribution of dopamine D_2 receptors is increased in the putamen in early Parkinson's disease (7).

The sigma receptor has been established as a distinct one, although it was initially proposed as a subtype of opioid receptors (8). It is classified into two subtypes, sigma$_1$ and sigma$_2$ (9). Sigma$_1$ receptor is considered to be involved in aging and various diseases, such as schizophrenia, depression, Alzheimer's disease and ischemia (10–14). Confirmed sigma$_1$ receptor ligand functions are neuroprotective, anti-amnestic and antidepressant (10, 15). Some studies suggested that sigma$_1$ receptors are involved in modulating the synthesis and release of dopamine (16, 17). However, the

relationship between the sigma$_1$ receptor and PD remains to be determined. The purpose of this study was to investigate the mapping of sigma$_1$ receptors in PD using [^{11}C]SA4503 (18–20) and PET scanning, and to assess whether sigma$_1$ receptors are involved in the damaged dopaminergic system in patients with PD.

Materials and methods

Subjects

We studied six patients with PD (two men and four women, mean age ± SD, 59.8 ± 14.3). Table 1 summarizes their clinical profiles. Diagnoses were based on their medical histories including the effectiveness of antiparkinsonian agents, physical and neurological examination, laboratory tests, and magnetic resonance imaging (MRI) study, after excluding other diseases (21, 22). To ensure the early diagnosis of PD, each patient was also examined for the distribution of dopamine transporters and dopamine D_2 receptors by PET scans, using [^{11}C]CFT and [^{11}C]RAC, respectively. We confirmed the low density of dopamine transporters and the normal or high density of dopamine receptors in the putamen of all patients (6, 23). The administration of antiparkinsonian agents was stopped 2 days before obtaining the PET scans. Patients in whom it was difficult to stop the medication temporarily were excluded from the study. To record the clinical severity of PD each patient was scored according to the Unified Parkinson's Disease Rating Scale (24) just before the first PET examination.

For [^{11}C]SA4503 PET scanning, the control group consisted of seven volunteers (two men and five women, age ± SD, 62.6 ± 8.2), without any history of neurological diseases or abnormalities on physical or neurological examinations. Another control group consisted of six volunteers (four men and two women, age ± SD, 64.5 ± 6.5) who underwent [^{11}C]CFT and [^{11}C]RAC PET scans. They were not currently receiving medications known to affect the brain metabolism. None had a history of alcoholism.

This study protocol was approved by the Ethics Committee of the Tokyo Metropolitan Institute of Gerontology. Prior written informed consent was obtained from all subjects participating in this study.

[^{11}C]CFT and [^{11}C]RAC PET

PET was performed in the Tokyo Metropolitan Institute of Gerontology Positron Medical Center with a HEADTOME V scanner (Shimadzu Co., Kyoto, Japan) (25). If the patients took antiparkinsonian agents, the administration of the agents was stopped 2 days before obtaining the PET scans.

[^{11}C]CFT was prepared as described before (26). The specific activity at the time of injection ranged from 16.9 to 82.4 GBq/μmol (39.6 ± 17.9 GBq/μmol). The transmission data were acquired with a rotating ^{68}Ga/^{68}Ge rod source for attenuation correction. Each subject received an intravenous injection of 300 MBq of [^{11}C]CFT. Starting 75-min post-injection, an emission scan was performed in the 3D mode for 15 min.

[^{11}C]RAC was prepared as described before (27). The specific activity at the time of injection ranged from 5.7 to 110.1 GBq/μmol (59.7 ± 30.7 GBq/μmol). The transmission data were acquired with a rotating ^{68}Ga/^{68}Ge rod source for attenuation correction. Each subject received an intravenous injection of 300 MBq of [^{11}C]RAC. Starting 40-min post-injection, an emission scan was performed in the 3D mode for 15 min.

[^{11}C]SA4503 PET

If the patients took antiparkinsonian agents, the administration of the agents was also stopped 2 days before obtaining the [^{11}C]SA4503 PET scan. [^{11}C]SA4503 was prepared as described before (18). The specific activity at the time of injection ranged from 23.7 to 282.6 GBq/μmol (104.6 ± 63.7 GBq/μmol). The transmission data were acquired with a

Table 1 Demographic and clinical data for patients with Parkinson's disease

ID	Age (years)	Sex	Symptom	Duration (years)	Medication before PET	Hoehn & Yahr	UPDRS
PD1	81	F	R > L	8	LDOPA selegiline	2	32
PD2	44	F	L > R	2.5	Selegiline	2	19
PD3	59	F	L > R	2	Selegiline	2	16
PD4	70	M	R > L	1.5	None	2	23
PD5	60	M	R > L	1	Trihexphenidyl	1	11
PD6	45	F	L > R	0.5	None	1	19

PD, Parkinson's disease; UPDRS, Unified Parkinson's Disease Rating Scale.

rotating $^{68}Ga/^{68}Ge$ rod source for attenuation correction. A dynamic series of decay-corrected PET data acquisition was performed in the 2D mode for 90 min starting at the time of the injection of 500 MBq of [^{11}C]SA4503. Arterial blood was sampled at 10, 20, 30, 40, 50, 60, 70, 80, 90, 100, 110, 120, 135 and 150 s, and at 3, 5, 7, 10, 15, 20, 30, 40, 50, 60, 75 and 90 min. Plasma was separated, weighed and measured for radioactivity with an NaI (Tl) well scintillation counter. Metabolite analysis was carried out by high-performance liquid chromatography (18).

Data analysis

Image manipulations were carried out on an O_2 workstation (Silicon Graphics Inc., Mountain View, CA, USA), using a medical image processing application package 'Dr View' version 5.2 (Asahi Kasei Joho System Co. Ltd, Tokyo, Japan).

In the [^{11}C]CFT and [^{11}C]RAC PET images, circular regions of interest (ROIs) 10 mm in diameter and extending over two slices of the images were drawn on the cerebellar hemisphere, head of caudate nucleus, and the anterior and posterior putamen. To evaluate dopaminergic function, we used the ROI value of striate body normalized by the cerebellar ROI value.

For [^{11}C]SA4503 PET, we generated early images for each subject by adding up the frames of the dynamic scan from 0 to 10 min (28). Circular ROIs 10 mm in diameter and extending over two slices of the images were drawn on the head of caudate nucleus, and the anterior and posterior putamen. The time-course of the tissue concentration of [^{11}C]SA4503 was computed from the PET data and the interpolated ROIs throughout the scanning period. A two-tissue two-compartment model was used to estimate k_1, k_2, k_3, k_4, and the delay between metabolite-corrected plasma and tissue time activity using a Gauss–Newton algorithm (13). The ratio of k_3 to k_4 was computed as the binding potential (BP), which is considered to be linearly related to the density of sigma$_1$ receptors.

Statistics

Unpaired t-tests were used to compare the BP in patients with PD and normal subjects. The Bonferroni correction was applied for multiple comparisons (three comparisons, corresponding to three regions). We also used the paired t-test with the Bonferroni correction to compare the more affected and the less affected side in the striatum of patients with PD. The level of significance was set at $P < 0.05$. The statistical computation was performed using a software package 'JMP' version 5.1.1 (SAS Institute Inc., Cary, NC, USA) on a Macintosh computer.

Results

Relative [^{11}C]CFT uptake of anterior and posterior putamen was significantly smaller in the patients

Table 2 Binding potential for sigma$_1$ receptors in each region in normal individuals and patients with Parkinson's disease

	[^{11}C]SA4503[a]		[^{11}C]CFT[b]		[^{11}C]RAC[b]	
Regions	Normal	PD	Normal	PD	Normal	PD
Head of caudate nucleus	12.0 ± 3.8	12.5 ± 7.0	3.55 ± 0.64	3.29 ± 0.38	3.82 ± 0.50	3.54 ± 0.37
Anterior putamen	12.2 ± 5.0	10.8 ± 4.2	3.86 ± 0.63	2.25 ± 0.45**	4.32 ± 0.54	4.84 ± 0.22
Posterior putamen	13.3 ± 4.7	13.1 ± 7.8	3.33 ± 0.51	1.74 ± 0.25***	3.97 ± 0.47	4.91 ± 0.42*

[a]Mean ± SD of binding potential (normal, $n = 7$; PD, $n = 6$).
[b]Mean ± SD of tissue count/cerebellar count (normal, $n = 6$; PD, $n = 6$).
*$P < 0.01$, **$P < 0.005$, ***$P < 0.001$ (unpaired t-test).

Table 3 Comparison of binding potential for sigma$_1$ receptors between the more and the less affected side of each region in six patients with Parkinson's disease

	[^{11}C]SA4503[a]		[^{11}C]CFT[b]		[^{11}C]RAC[b]	
Regions	More affected	Less affected	More affected	Less affected	More affected	Less affected
Head of caudate nucleus	14.3 ± 10.0	10.8 ± 5.6	3.21 ± 0.36	3.36 ± 0.42	3.55 ± 0.54	3.53 ± 0.33
Anterior putamen	9.1 ± 4.4	12.4 ± 4.3*	2.00 ± 0.38	2.50 ± 0.54*	5.03 ± 0.30	4.65 ± 0.24
Posterior putamen	12.4 ± 8.2	13.7 ± 8.0	1.55 ± 0.14	1.93 ± 0.41	5.15 ± 0.73	4.68 ± 0.47

[a]Mean ± SD of binding potential ($n = 6$).
[b]Mean ± SD of tissue count/cerebellar count ($n = 6$).
*$P < 0.05$ (paired t-test).

with PD than in the controls (Table 2). The [^{11}C]RAC uptake of posterior putamen was significantly larger in the patients than in the controls (Table 2). In PD patients, the [^{11}C]CFT uptake was significantly lower on the more affected than the less affected side of the anterior putamen (Table 3).

There was no significant difference with respect to the BP for [^{11}C]SA4503 between PD patients and the controls (Table 2). In PD patients, the BP was significantly lower on the more affected than the less affected side of the anterior putamen (Table 3).

Discussion

Symptoms first manifest unilaterally in most PD patients, although they begin symmetrically in other movement disorders (22, 29). We draw attention to this asymmetry in PD. Our results demonstrate that in PD, the binding ability of sigma$_1$ receptors was lower on the more affected than the less affected side of the anterior putamen. We propose that if sigma$_1$ receptors exist only in the presynaptic part of dopaminergic synapses, our results reflect the degeneration of dopaminergic neurons in the substantia nigra. Past studies indicate, however, that sigma$_1$ receptors are active within both presynaptic and postsynaptic neurons (17, 30, 31). In patients with PD, the release of dopamine in the putamen is reduced. Chaki et al. suggested that sigma$_1$ binding sites are involved in modulating the release of dopamine by interacting with NMDA receptors on dopaminergic nerve terminals (17). Release of dopamine is reduced in the putamen with PD. Sigma$_1$ receptor may be down-regulated in the putamen with PD, as well as DAT (5).

Our data suggest that [^{11}C]SA4503 PET is an indicator of presynaptic dopaminergic damage in PD. In both controls and patients, however, dispersion between the individual distribution volumes of sigma$_1$ receptor was large in the striate body. Unfortunately, we cannot say that [^{11}C]SA4503 PET is suitable for early diagnosis of PD. We have interest in the relationship between sigma$_1$ receptor and the side effects of antiparkinsonian agents. Further studies will be needed, such as comparison between sigma$_1$ receptor function in a *de novo* PD group and in an advanced group of PD patients with a long-term levodopa treatment.

Acknowledgements

This work was supported by a Grant-in-Aid for Scientific Research (B) No. 13557077 from the Ministry of Education, Culture, Sports, Science and Technology, Japan. The authors thank Ms M. Ando taking care of the subjects undergoing PET scanning.

References

1. Dauer W, Przedborski S. Parkinson's disease: mechanisms and models. Neuron 2003;**39**:889–909.
2. Michell AW, Lewis SJG, Foltynie T, Barker RA. Biomarkers and Parkinson's disease. Brain 2004;**127**:1693–705.
3. Morrish PK, Sawle GV, Brooks DJ. Regional changes in [^{18}F]dopa metabolism in the striatum in Parkinson's disease. Brain 1996;**119**:2097–103.
4. Rinne JO, Laihinen A, Nagren K, Ruottinen H, Ruotsalainen U, Rinne UK. PET examination of the monoamine transporter with [^{11}C]beta-CIT and [^{11}C]beta-CFT in early Parkinson's disease. Synapse 1995;**21**:97–103.
5. Lee CS, Samii A, Sossi V et al . In vivo positron emission tomographic evidence for compensatory changes in presynaptic dopaminergic nerve terminals in Parkinson's disease. Ann Neurol 2000;**47**:493–503.
6. Ribeiro MJ, Vidailhet M, Loc'h C et al . Dopaminergic function and dopamine transporter binding assessed with positron emission tomography in Parkinson disease. Arch Neurol 2002;**59**:580–6.
7. Rinne JO, Laihinen A, Ruottinen H et al . Increased density of dopamine D2 receptors in the putamen, but not in the caudate nucleus in early Parkinson's disease: a PET study with [^{11}C]raclopride. J Neurol Sci 1995;**132**:156–61.
8. Walker JM, Bowen WD, Walker FO, Matsumoto RR, De Costa B, Rice KC. Sigma receptors: biology and function. Pharmacol Rev 1990;**42**:355–402.
9. Quirion R, Bowen WD, Itzhak Y et al . A proposal for the classification of sigma binding sites. Trends Pharmacol Sci 1992;**13**:85–6.
10. Maurice T, Urani A, Phan VL, Romieu P. The interaction between neuroactive steroids and the sigma$_1$ receptor function: behavioral consequences and therapeutic opportunities. Brain Res Rev 2001;**37**:116–32.
11. Lobner D, Lipton P. Sigma-ligands and non-competitive NMDA antagonists inhibit glutamate release during cerebral ischemia. Neurosci Lett 1990;**117**:169–74.
12. Matsuno K, Kobayashi T, Tanaka MK, Mita S. Sigma 1 receptor subtype is involved in the relief of behavioral despair in the mouse forced swimming test. Eur J Pharmacol 1996;**312**:267–71.
13. Kawamura K, Kimura Y, Tsukada H et al . An increase of sigma receptors in the aged monkey brain. Neurobiol Aging 2003;**24**:745–52.
14. Ishiwata K, Kobayashi T, Kawamura K, Matsuno K. Age-related changes of the binding of [^{3} H]SA4503 to sigma1 receptors in the rat brain. Ann Nucl Med 2003;**17**:73–7.
15. Bowen WD. Sigma receptors: recent advances and new clinical potentials. Pharm Acta Helv 2000;**74**:211–8.
16. Booth RG, Baldessarini RJ. (+)-6,7-benzomorphan sigma ligands stimulate dopamine synthesis in rat corpus striatum tissue. Brain Res 1991;**557**:349–52.
17. Chaki S, Okuyama S, Ogawa S, Tomisawa K. Regulation of NMDA-induced [^{3}H]dopamine release from rat hippocampal slices through sigma-1 binding sites. Neurochem Int 1998;**33**:29–34.
18. Kawamura K, Ishiwata K, Tajima H et al . In vivo evaluation of [^{11}C]SA4503 as a PET ligand for mapping CNS sigma$_1$ receptors. Nucl Med Biol 2000;**27**:255–61.
19. Ishii K, Ishiwata K, Kimura Y, Kawamura K, Oda K, Senda M. Mapping of sigma$_1$ receptors in living human brain. NeuroImage 2001;**13**:S984.

20. Ishiwata K, Tsukada H, Kawamura K et al . Mapping of CNS sigma$_1$ receptors in the conscious monkey: preliminary PET study with. Synapse 2001;**40**:235–7.
21. Koller WC, Montgomery EB. Issues in the early diagnosis of Parkinson's disease. Neurology 1997;**49**(Suppl. 1):S10–25.
22. Gelb DJ, Oliver E, Gilman S. Diagnostic criteria for Parkinson disease. Arch Neurol 1999;**56**:33–39.
23. Kaasinen V, Ruottinen HM, Nagren K, Lehikoinen P, Oikonen V, Rinne JO. Upregulation of putaminal dopamine D_2 receptors in early Parkinson' disease: a comparative PET study with [^{11}C] raclopride and [^{11}C]N-methylspiperone. J Nucl Med 2000;**41**:65–70.
24. Fahn S, Elton RL. Committee MoUd. Unified Parkinson's disease rating scale. In: Fahn S, Marsden CD, Calne DC, Goldstein M, eds. Recent development in Parkinson's disease, Vol. 2. New Jersey: Macmillan Healthcare Information, 1987;153–64.
25. Fujiwara T, Watanuki S, Yamamoto S et al . Performance evaluation of a large axial field-of-view PET scanner: SET-2400W. Ann Nucl Med 1997;**11**:307–13.
26. Kawamura K, Ishiwata K, Futatsubashi M et al . Efficient HPLC separation of [^{11}C]beta-CFT or [^{11}C]beta-CIT from an N-desmethyl precursor on a semipreparative reversed phase ODS column. Appl Radiat Isot 2000;**52**:225–8.
27. Ishiwata K, Ishii S, Senda M. An alternative synthesis of [^{11}C]raclopride for routine use. Ann Nucl Med 1999;**13**:195–7.
28. Mishina M, Senda M, Kimura Y et al . Intrasubject correlation between static scan and distribution volume images for [^{11}C]flumazenil PET. Ann Nucl Med 2000;**14**:193–8.
29. Hughes AJ, Ben-Shlomo Y, Daniel SE, Lees AJ. What features improve the accuracy of clinical diagnosis in Parkinson's disease: a clinicopathologic study. Neurology 1992;**42**:1142–6.
30. Gonzalez-Alvear GM, Werling LL. Regulation of [^{3}H]dopamine release from rat striatal slices by sigma receptor ligands. J Pharmacol Exp Ther 1994;**271**:212–9.
31. Alonso G, Phan V, Guillemain I et al . Immunocytochemical localization of the sigma$_1$ receptor in the adult rat central nervous system. Neuroscience 2000;**97**:155–70.

Journal of Computer Assisted Tomography
27(2):241–248
© 2003 Lippincott Williams & Wilkins, Inc., Philadelphia

Magnetic Resonance Imaging Findings of Machado–Joseph Disease: Histopathologic Correlation

Aya M. Tokumaru, Keiko Kamakura, Toshiyuki Maki, Shigeo Murayama, Ikuko Sakata, Tatsumi Kaji, Shinnya Kohyama, Shoichi Kusano, and Seiji Hasegawa

Purpose: To determine the characteristic magnetic resonance imaging (MRI) findings of early- and late-stage Machado–Joseph disease (MJD) and to examine correlation with pathologic specimens.

Patients and Methods: Four patients genetically diagnosed with MJD and a familial case of MJD were all examined using MRI. Machado–Joseph disease was pathologically confirmed in one of the four genetically diagnosed patients, and the findings were compared with the MRI results.

Results: In all three patients who had MJD for less than 8 years, MRI confirmed mild cerebellar atrophy, particularly in the vermis, and atrophic changes in the superior cerebellar peduncle. Mild pontine atrophy was observed in these three patients. Atrophic changes in the pontine tegmentum were more prominent than those of the pontine base in these patients. Two of the three patients showed mild frontal atrophy. Of the five total patients, two had the disease for over 10 years and showed progressive atrophy of the brainstem and mild frontal atrophy. These two patients also showed pallidal atrophy. One autopsied case in which the disease duration was 17 years showed a typical pathologic picture of MJD. Macroscopic findings for this patient showed marked atrophy of the pons, mild cerebellar atrophy (particularly in the vermis), marked atrophy of the superior cerebellar peduncle, severe involvement of motor nuclei, and atrophy and discoloration of the pallidum and subthalamic nuclei.

Conclusion: In the early stages of MJD, mild pontine atrophy, particularly in the tegmentum, and mild cerebellar atrophy are typical MRI findings. Atrophic changes in the brainstem may be progressive. Pallidal atrophy may be observed in patients with long disease duration. These findings correlated with the pathologic findings.

Index Terms: Machado–Joseph disease—Spinocerebellar degeneration—Magnetic resonance imaging—Histopathologic correlation.

Machado–Joseph disease (MJD) is an autosomal dominant, multisystem, neurodegenerative disorder originally reported in Portuguese-Azorean families (1,2). Recently, MJD has been reported in non–Portuguese-Azorean families worldwide (3,4) and is considered the most common type of autosomal dominant spinocerebellar degeneration. Pathologically, marked degeneration is observed in the subthalamopallidal (inner segment) system, the dentatorubral system, and the nuclei of cranial nerves. In contrast, the cerebral cortex, thalamus, inferior olivary nucleus, cerebellar cortex, and corticospinal tract are mostly preserved. Machado–Joseph disease can be readily differentiated from other spinocerebellar degenerations based on these pathologic characteristics (5,6). Clinically, MJD is characterized by spasticity, cerebellar ataxia, characteristic facial features, muscle atrophy, and dystonia. Clinical symptoms vary widely among different ages at onset, however, and in the past, the disease concept of MJD was confused with that of dentatorubropallidoluisisan atrophy (DRPLA). Differentiation is still clinically problematic in many cases (7). Advances in genetic analysis have made it possible to diagnose MJD more accurately (8,9). Takiyama et al. (8) determined that MJD has an abnormal genetic locus at 14q. Recent progress in imaging diagnosis, particularly in magnetic resonance imaging (MRI), has allowed detailed evaluations of the cerebellum and brainstem, providing

From the Departments of Radiology (A. M. Tokumaru, I. Sakata, T. Kaji, S. Kohyama, and S. Kusano), and Internal Medicine (K. Kamakura), National Defense Medical College, Saitama, Department of Neurology, Kameda Medical Center, Chiba (T. Maki and S. Hasegawa), and Department of Neuropathology, Tokyo Metropolitan Institute of Gerontology, Tokyo (S. Murayama), Japan.

Address correspondence and reprint requests to Dr. A. M. Tokumaru, Department of Radiology, National Defense Medical College, 3-2 Namiki, Tokorozawa-City, Saitama, Japan. E-mail: ayasan@ me.ndmc.ac.jp

useful information for diagnosing and differentiating spinocerebellar degenerations. Only a few studies have examined imaging and MRI of MJD, however (10,11). Therefore, we determined the characteristic MRI findings of MJD, especially in the early stages, and detected changes according to the disease process. Our study is the first to correlate MRI findings with pathologic features.

PATIENTS AND METHODS

Patients

Our patient population consisted of four women and one man between the ages of 26 and 56 years. Four patients had been genetically diagnosed with MJD, and the other was the mother of one of the genetically diagnosed patients. Age at onset of disease was between 20 and 28 years. The disease duration was 4 to more than 30 years. The disease duration was less than 8 years in three patients and over 10 years in the other two. We observed all patients for 4 to 7 years. Patient details are shown in Table 1. The mean age of controls in the study by Murata et al. (10) was higher than that of the early-stage group, and the slice orientation of the axial and coronal images is different from our data. Therefore, we also studied 21 age-matched control subjects without intracranial lesions (21 women; mean ± SD: 33.8 ± 3.4 years) to compare the results of the patients whose disease duration was less than that of the patients with early-stage disease.

Methods

Transaxial T1-weighted (repetition time/echo time = 600/15 ms) and dual-echo T2-weighted (repetition time/echo time = 3,500/120/20) MRI in 3–5-mm thick sections and sagittal and coronal T1- or T2-weighted images in 5-mm thick sections were obtained using a 1.5-T GE Medical Systems MRI unit. Measurements were performed separately by three neuroradiologists (A. M. T., T. K., and S. K.). Fifteen measurements were taken according to the method described Murata et al. (10), and the area of the pontine tegmentum was measured on medial sagittal MRI scans according to the method described by Etchebehere et al. (12). Figure 1 shows the 15 measurements, which were as follows: 1) anteroposterior diameter of the globus pallidus, 2) transverse diameter of the globus pallidus, 3) anteroposterior diameter of the midbrain, 4) transverse diameter of the midbrain, 5) width of the superior cerebellar peduncles, 6) width of middle cerebellar peduncle, 7) diameter of the dentate nucleus, 8) diameter of the red nucleus, 9) anteroposterior diameter of the pons, 10) transverse diameter of the pons, 11) anteroposterior diameter of the fourth ventricle, 12) transverse diameter of the fourth ventricle, 13) anteroposterior diameter of the medullar oblongata, 14) transverse diameter of the medullar oblongata, and 15) area of the cerebellum.

To analyze neuroanatomic details in the brainstem as accurately as possible, we made a slice in a direction either parallel or perpendicular to the long axis of the brainstem in the early-stage cases. In the article by Murata et al. (10), the orbitomeatal line was probably selected and the mean age of controls was higher than that of early-stage group in our data. Therefore, for evaluating the data on the patients in the early stage of the disease, we made the new control data. The slice orientation of our patients in the late stage (patients 4 and 5) was the orbitomeatal line; thus, they were compared with the data in the studies by Murata et al. (10) and Onodora et al. (15).

One patient was pathologically confirmed to have MJD at autopsy, and the histologic findings were then compared with the MRI findings.

RESULTS

Table 2 shows the results of the various measurements. A comparison of the MRI findings of the three patients who had MJD with a disease duration of less than 8 years with the control group revealed that the anteroposterior diameter of the pons, the transverse diameter of the midbrain, and the transverse and anteroposterior diameters of the fourth ventricle were smaller

TABLE 1. *Clinical presentation of the patients*

Patient number	Sex	Age at MR exam (years)	Disease duration	Clinical symptoms at MR exam	Genetic analysis	CAG repeats
1	F	26	4	Ataxia, dystonia,	+	14/76
		28	6	saccadic eye movement athetose, need assistance in walking		
2	F	31	5	Saccadic eye movement nystagmus, divergence dystonia, athetose, ataxia urinary incontinence unable to walk, need assistance in standing	+	14/79
3	M	30	8	Nystagmus, dystonia ataxia, nystagmus, ataxia need assistance in walking	+	14/77
4	F	38	10	Aphonia, need assistance in standing unable to walk		
		43	15	Dysarthria, slow saccade dystonia, nystagmus, no ataxia		
		45	17	Vertical eye movement disorder, slow saccade dyskinesia in face dystonia, no ataxia, bulbar palsy, bedridden	+	14/77
5	F	55	32	Bedridden, ataxia, DTR(−) slow eye movement	Mother of patient 3	−

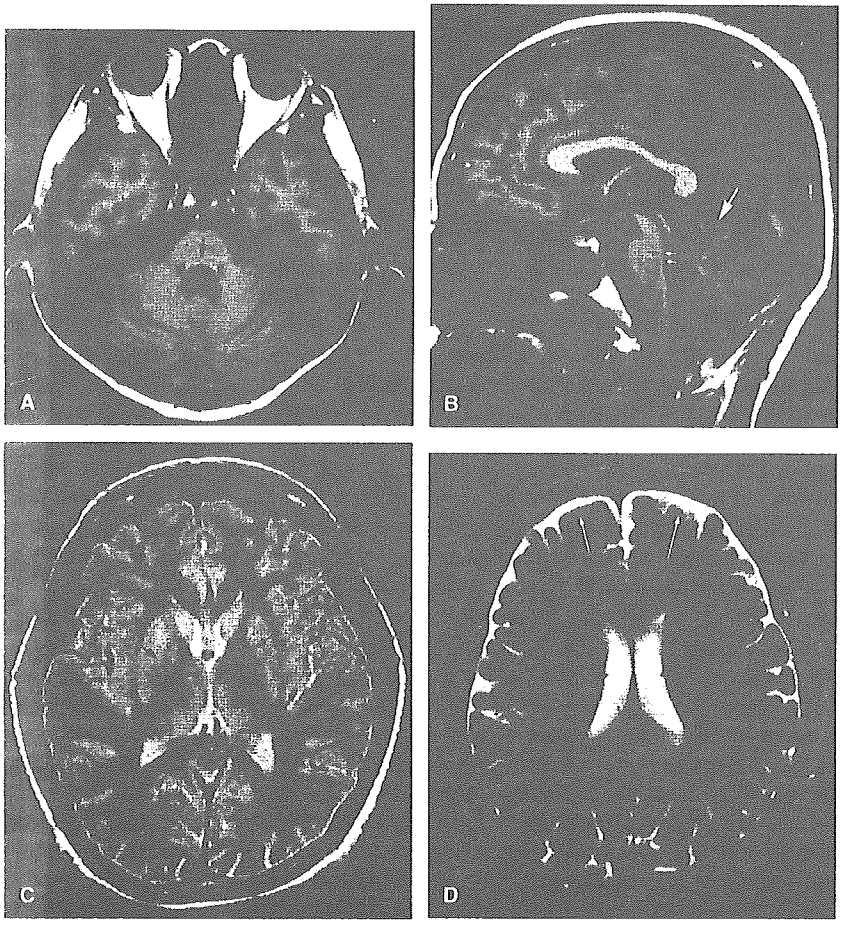

FIG. 1. Patient 1, a 28-year-old woman with Machado–Joseph disease with a disease duration of 6 years. **A:** Axial T1-weighted image (600/15) shows dilatation of the fourth ventricle (arrow). **B:** Sagittal T1-weighted image shows mild cerebellar atrophy for her age, especially in the vermis (arrow). Area of dorsal pons is smaller than that of control data, suggesting atrophic change of the pontine tegmentum (small black and white arrow). **C:** Axial proton density image (3000/17) shows no significant atrophic change in the globus pallidus (arrow). **D:** Axial T2-weighted image (3000/120) shows mild frontal atrophy (arrow).

TABLE 2. *MRI findings*

Patient number (disease duration, y)	1 (4)	2 (5)	3 (8)	Control (n = 21)	4 (10)	4 (17)	5 (32)	Control 2 (data from reference 10 and 15)
Findings								
Pons, cm								
AP	2.12	1.84*	1.92*	2.21 ± 0.23	2.11†	1.87†	1.94†	2.47 ± 0.21
Trans	2.97	2.54*	2.98*	3.18 ± 0.24	2.54†	2.48†	2.29†	3.00 ± 0.25
Midbrain, cm								
AP	2.51	2.4*	2.54*	2.67 ± 0.18	1.98†	1.90†	2.05†	2.62 ± 0.16
Trans	2.98*	3.01*	3.11*	3.42 ± 0.25	2.94†	2.88†	3.12†	3.59 ± 0.40
Medulla oblongata								
AP	1.54	1.48	1.34	1.42 ± 0.23	1.32†	1.34†	1.34†	1.66 ± 0.25
Trans	1.41	1.84	1.72	1.67 ± 0.19	1.5†	1.52†	1.43†	1.72 ± 0.16
Fourth ventricle, cm								
AP	1.12*	1.78*	1.8*	0.86 ± 0.24	1.75†	1.80†	1.56†	1.11 ± 0.26
Trans	1.50*	1.82*	1.84*	1.12 ± 0.38	1.81†	1.84†	1.76	1.44 ± 0.37
Middle cerebellar peduncle, cm	1.35	1.42	1.39	1.49 ± 0.32	1.21†	1.18†	1.13†	1.79 ± 0.24
Superior cerebellar peduncle, cm	1.84	1.68*	1.71*	2.02 ± 0.14	1.52†	1.50†	1.46†	2.00 ± 0.12
Dentate nucleus, cm	1.45	1.48	1.4	1.59 ± 0.22	1.73	1.65†	1.63	1.54 ± 0.22
Red nucleus, cm	0.54	0.52	0.48	0.54 ± 0.14	0.60	—	0.59	0.69 ± 0.11
Globus pallidus, cm								
AP	2.21	2.32	2.18	2.21 ± 0.23	2.34	2.30	2.28	2.54 ± 0.37
Trans	0.78	0.64	0.6	0.68 ± 0.21	0.65†	0.60†	0.68†	0.83 ± 0.16
Areas of cerebellum, cm^2	38.45	36.34	35.45	39.35 ± 5.64	34.38†	35.29†	36.54†	41.45 ± 6.47
Area of ventral pons, cm^2	3.4	3.21	3.19	3.44 ± 0.39	2.78†	2.67†	2.59†	3.56 ± 0.48
Area of dorsal pons, cm^2	1.48*	1.49*	1.5*	1.69 ± 0.18	1.29†	1.19†	1.34†	1.71 ± 0.17

* >Control ± 1SD.
† Atrophy matching with Machado-Joseph disease in references 10 and 15.

in our patients with MJD (see Fig. 1A). Although mild pontine atrophy, particularly in the tegmentum (see Fig. 1B), and atrophic changes of the superior cerebellar peduncle were seen, these decreases were milder numerically when compared with those in the MJD group in the study by Murata et al. (10). Furthermore, a mild decrease in the area of the cerebellum was evident, but it was easy to macroscopically detect enlarged cerebellar folia. In addition, a cross-shaped high-intensity area in the pons suggesting degenerative changes was observed in four patients but remained mild.

In all three tests for the two patients who had MJD for 10 years or longer, atrophy matching the MJD patients in the study by Murata et al. (10) was evident. In other words, the two patients with MJD for more than 15 years showed severe pontine atrophy, including in the pontine base and tegmentum (Fig. 2A–D). Subtle degenerative changes in the pontine transverse fibers were observed (see Fig. 2C). Atrophic changes in the superior cerebellar peduncle were prominent (see Fig. 2F). The cerebellum showed mild atrophy without progression, particularly in the vermis, compared with those patients with shorter disease duration. Patient 4, who was followed for 7 years at our institute, showed progressive pontine atrophy (see Fig. 2D; Table 2). The cerebellar atrophy was not as progressive as pontine atrophy, however. Atrophic changes in the globus pallidus were observed in these two patients (see Fig. 2E). Detection of any degenerative changes in motor nuclei in the brainstem and subthalamic nuclei was difficult using MRI.

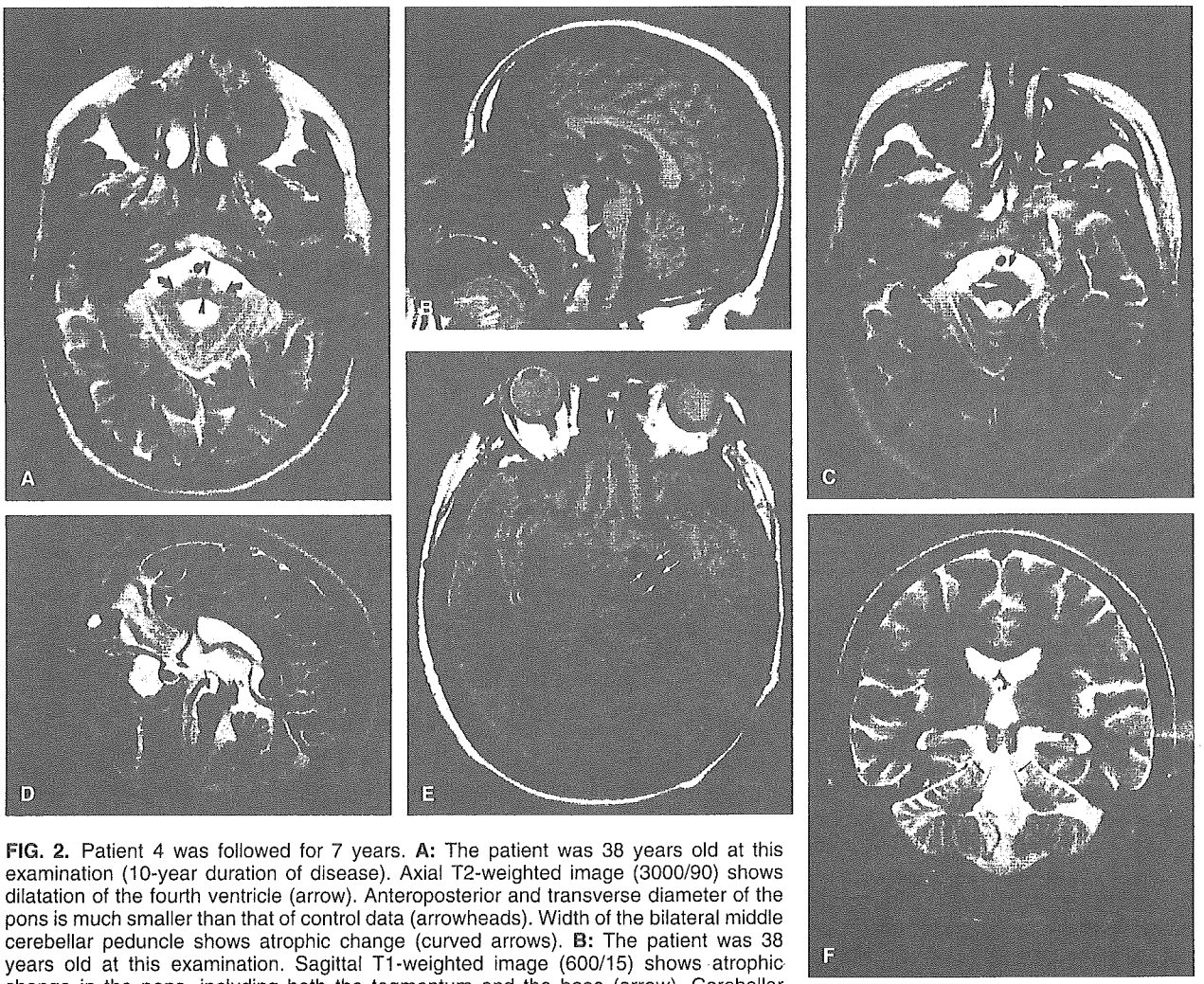

FIG. 2. Patient 4 was followed for 7 years. **A:** The patient was 38 years old at this examination (10-year duration of disease). Axial T2-weighted image (3000/90) shows dilatation of the fourth ventricle (arrow). Anteroposterior and transverse diameter of the pons is much smaller than that of control data (arrowheads). Width of the bilateral middle cerebellar peduncle shows atrophic change (curved arrows). **B:** The patient was 38 years old at this examination. Sagittal T1-weighted image (600/15) shows atrophic change in the pons, including both the tegmentum and the base (arrow). Cerebellar atrophy was mild. **C, D:** The patient was 45 years old at this examination (17-year disease duration). Axial T2-weighted image (3000/90) and sagittal T2-weighted image (600/15) show progressive pontine atrophy (black arrows). Cerebellar atrophy was not as progressive as the pontine appearance. Linear hyperintensity lesion is shown in the midline of the pons (**C**, white arrow), suggesting mild degenerative change of pontine transverse fibers. This finding is compatible with the pathologic feature demonstrated in (**K**). **E:** The patient was 45 years old at this examination. Axial proton density image (3000/15) shows a decrease in size of the globus pallidus (arrow). **F:** The patient was 45 years old at this examination. Coronal T2-weighted image (3000/90) shows atrophic change of the superior cerebellar peduncles (arrow). Continued.

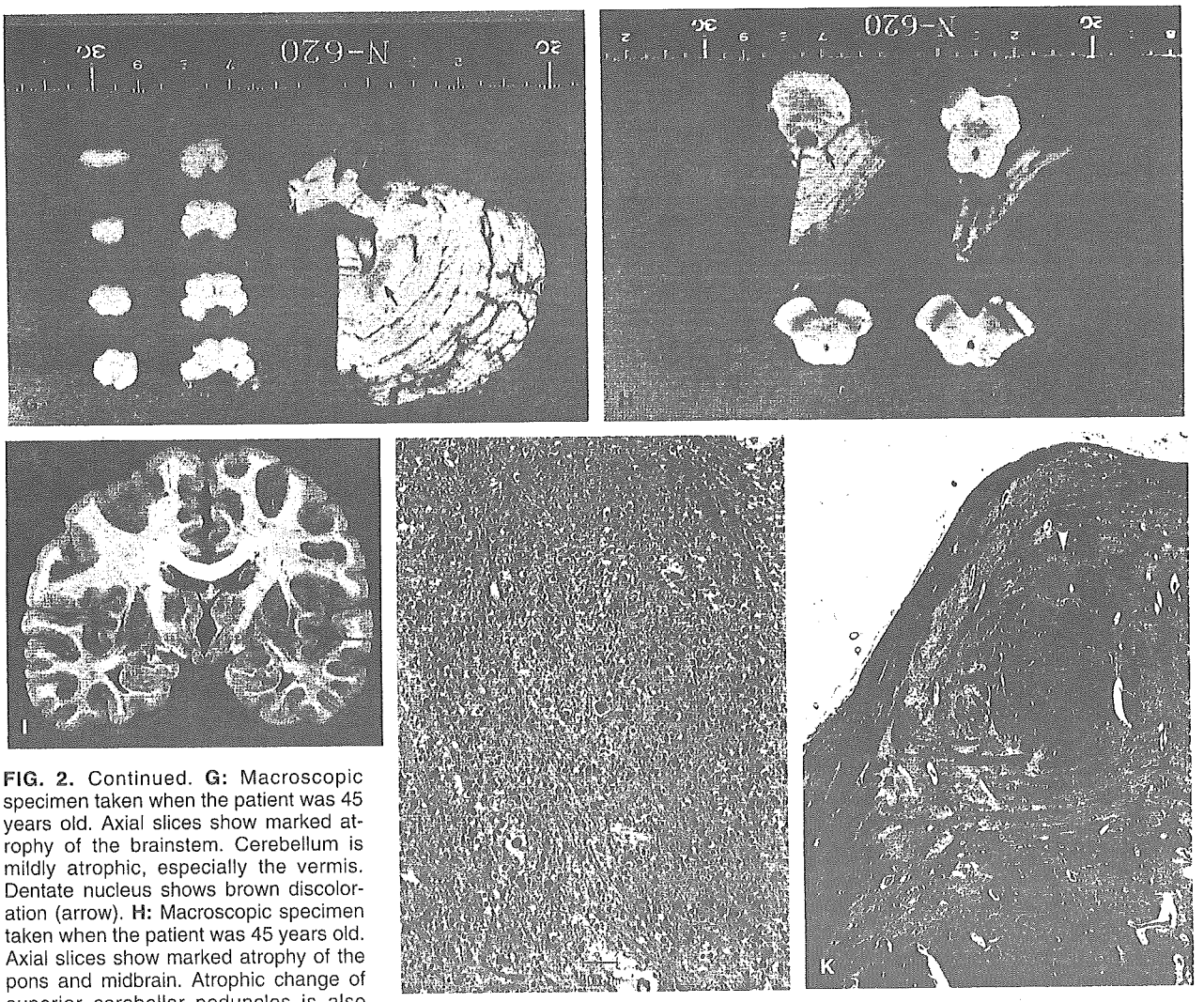

FIG. 2. Continued. **G:** Macroscopic specimen taken when the patient was 45 years old. Axial slices show marked atrophy of the brainstem. Cerebellum is mildly atrophic, especially the vermis. Dentate nucleus shows brown discoloration (arrow). **H:** Macroscopic specimen taken when the patient was 45 years old. Axial slices show marked atrophy of the pons and midbrain. Atrophic change of superior cerebellar peduncles is also shown (arrows). **I:** Coronal slice of the brain shows atrophy with brown discoloration of the pallidum (arrow) and subthalamic nuclei (small arrow). **J:** Histologic specimen (hematoxylin–eosin stain × 50) of the globus pallidus shows apparent increase in the density of oligodendroglias (arrow). **K:** Histologic specimen (hematoxylin–eosin stain × 3.14) of the pontine base demonstrates moderate loss of pontine crossing fibers (arrow), with marked preservation of corticospinal tracts (arrowhead).

Histopathology

The autopsy report of patient 4 showed marked atrophy of the pons. The cerebellum was mildly atrophic, particularly in the vermis. The fourth, fifth, seventh, and eleventh cranial nerves were atrophic. Serial coronal slices of the brain showed atrophy with brown discoloration of the pallidum and subthalamic nuclei. Serial axial slices of the brainstem and the right cerebellum showed a moderate change in the pigment of the substantia nigra, marked atrophy of the superior cerebellar peduncles, diffuse atrophy at the base of the pons, and relative preservation of the bilateral pyramidal tracts. Serial sagittal slices of the left cerebellum showed brown discoloration of the dentate nucleus and atrophy of the superior cerebellar peduncle.

Histologic examination of the basal ganglia and thalamus showed marked atrophy of the inner segment of the pallidum and the subthalamic nucleus, with an apparent increase in the density of oligodendroglias. These changes are characteristic of MJD. The degenerative changes in the outer segment of the pallidum were milder than those in the inner segment. The thalamus and hypothalamus were unremarkable.

In the midbrain, the primary oculomotor nuclei showed moderate neuronal loss and gliosis. Edinger-Westphal nuclei were relatively well preserved. The substantia nigra and the red nucleus showed mild gliosis. The cerebral peduncle was unremarkable. In the pons, there was moderate neuronal loss and gliosis in the fifth, sixth, and seventh cranial motor nuclei. The base of the pons showed moderate loss of pontine crossing fibers with marked preservation of corticospinal tracts. In the

medulla oblongata, hypoglossal nuclei showed neuronal loss with moderate gliosis.

In the cerebellum, the cerebellar cortex was unremarkable. Purkinje cells were well preserved. Cerebellar white matter did not show gliosis. The dentate nucleus showed a marked grumous alteration. This case presented a typical pathologic picture of MJD: a pattern of subthalamopallidal degeneration, severe involvement of cranial motor nuclei, prominent grumous alteration of the dentate nucleus, and atrophy of the cervical and thoracic anterolateral funiculus.

In Table 3, a comparison between the pathologic findings and the imaging findings is shown. The MRI findings of the distribution of the atrophic changes such as atrophy in the vermis, globus pallidus, and superior cerebellar peduncle were consistent with the macroscopic findings observed in the autopsy case. It was difficult to depict degeneration and atrophy of the cranial motor nuclei and cranial nerves in MRI, however.

DISCUSSION

Recent advances in genetic analysis have enabled the accurate diagnosis of MJD (8,9,13,14). Nevertheless, imaging analysis, particularly MRI, could provide useful information for the differential diagnosis, provide a more accurate picture of the distribution of degenerative foci, and produce the changing pattern according to the clinical course. In cases in which genetic diagnosis is rejected on ethical grounds, MRI could become one of the most important diagnostic tools.

Although only five cases were examined in the current study, including a familial case, we consider slight atrophy of the brainstem, atrophy of the pontine tegmentum and the superior cerebellar peduncle, and slight atrophy of the cerebellar vermis to be characteristic of MJD with an 8-year or shorter duration of disease, showing the main symptoms of ataxic gait, nystagmus, and increased tendon reflex. Previous reports on the imaging findings for MJD have documented progression based on disease stage or CAG expansion (11,15). The current study is the first to document that at a certain stage of MJD, although clinical findings are severe, imaging findings can be mild, to present the imaging findings for not only the posterior cranial fossa but also the basal ganglia and frontal lobe atrophy, and to report changes in imaging findings matching pathologic findings at different stages of MJD in one patient. These MRI findings were so subtle that they almost escaped notice. Clinically, it was sometimes difficult to differentiate MJD from other spinocerebellar degenerations, even in the early stages. Because the efferent dentatorubral system, where degeneration of MJD is localized, passes through the superior cerebellar peduncle, it is important to note these subtle findings of MJD with shorter disease duration.

The clinical symptoms of MJD are slowly progressive. Palsies of the extraocular muscles, muscular atrophy, and dystonia developed in the present cases, which included a patient in whom the entire course of the disease could be followed. In the two patients with MJD of 10 years' duration or longer, autonomic disturbances were also observed. In these two patients, brainstem atrophy markedly progressed, whereas progression of cerebellar atrophy was only slight compared with that of the brainstem. Progression of the fourth ventricular dilation was also detected, and superior cerebellar peduncular atrophy was marked. In these two patients, atrophy of the globus pallidus was observed, but the inner-outer segments were hardly distinguishable. The clinical symptoms were progressive, and atrophy of the brainstem and globus pallidus detected by imaging was also progressive. In the current study, the degree of these changes and their progression are most likely a result of the duration of the disease.

Genetic neurodegenerative disorders, including MJD, are associated with abnormal CAG repeat expansions. The results of biochemical analyses on proteins produced

TABLE 3. *Comparison between pathologic and imaging findings*

Modality	MR imaging findings	Pathologic findings
Findings		
Atrophy		
Pons	++	++
Cerebellum	+	+
Superior cerebellar peduncle	++	++
Inner segment of the pallidum	+	+
Subthalamic nucleus	Unknown	+
Fourth, fifth, and eleventh nerves	Unknown	+
Degeneration		
Inner segment of the pallidum	Unknown	Discoloration, oligodendroglia ⇑
Subthalamic nuclei	Unknown	Discoloration, oligodendroglia ⇑
Dentate nucleus	Unknown	Discoloration
Principal oculomotor nuclei	Unknown	Moderate neuronal loss and gliosis
Substantia nigra and red nucleus	Unknown	Mild gliosis
Fifth, sixth and seventh cranial nerves	Unknown	Moderate neuronal loss and gliosis
Pontine crossing fibers	+	Moderate loss

+, mild atrophy; ++, moderate to marked atrophy; ⇑, oligodendroglia markedly increased in inner segment of pallidum and subthalamic nuclei.

by expanded CAG repeats and the results of phenotype analyses using transgenic mice having mutated genes have shown the polyglutamate chains, which are the products of the translation of expanded CAG repeats, cause neuronal death. With these mice, the degree of expansion increases to hasten the age of onset and to exacerbate clinicopathologic findings with each generation, thus suggesting a relation between CAG repeats and anticipation of disease. Etchebehere et al. (12) performed MRI and brain single-photon emission computed tomography on 12 patients with MJD and documented a correlation between the length of CAG repeats and reduced perfusion in the parietal lobe, cerebellar vermis, and lateral temporal lobe. Furthermore, the results of a few recent reports have suggested that the severity of imaging findings is not necessarily based on the number of CAG repeats alone but on multiple factors such as age and disease stage (11,15). Because of the limited number of cases in the current study, correlation of the MRI findings with the size of expanded CAG repeats was not possible. Comparison with the degree of abnormality in the gene locus, particularly in CAG repeat expansion, and comparison with clinical symptoms and imaging findings are important foci for further investigation. Furthermore, because the possibility exists that expanded CAG repeats can hasten the exacerbation of MJD, more patients need to be studied. The imaging findings of the distribution of the atrophic changes such as atrophy in the vermis and superior cerebellar peduncular atrophy were consistent with the macroscopic findings observed in the autopsy case. Direct depiction of degeneration and atrophy of the cranial motor nuclei and cranial nerves is difficult in MRI, which may be a result of limited spatial resolution. Atrophy of the globus pallidus was detected in cases with prolonged disease duration and was considered to correspond to pathologic findings. The inner-outer segments were difficult to distinguish, however, and atrophy of the inner segment, which is thought to be characteristic of this disease, was barely captured by imaging. It was also difficult to capture features of the subthalamic nucleus and dentate nucleus by imaging, suggesting that improvement in contrast and spatial resolution may improve evaluation. Thus, it is difficult to describe frontal atrophy as a definitive characteristic of this disease, although it is consistent with pathologic observations.

Recent studies have greatly facilitated the classification of autosomal dominant spinocerebellar ataxia (SCA). Analysis of linkage in large families with SCA has assigned gene foci to at least eight chromosomes. One gene is located in the short arm of chromosome 6 and causes SCA type 1 (SCA1) (16). A gene in the long arm of chromosome 14 underlies MJD (8,9). A third gene locus is assigned to the short arm of chromosome 12, causing DRPLA (17,18). The gene for SCA2 is located at 12q23-24 (19). Subsequently, a sporadic counterpart of hereditary olivopontocerebellar atrophy (OPCA) of the Menzel type has been clearly defined (SCA2), and all these syndromes (nonhereditary OPCA, striatonigral degeneration, and Shy–Drager syndrome) are now classified as multiple system atrophy. In SCA2, the OPCA lesions are comparable to those in multiple system atrophy. The eponyms of both Dejerine–Thomas and of Menzel have been applied based on the similarity of pathologic changes in the olivopontocerebellar system. Unfortunately, even cases with milder OPCA lesions have been classified as OPCA. Thus, until recently, many cases of SCA1 and SCA3 have been vaguely grouped as hereditary OPCA (20).

Only a few studies on MRI of SCA have performed correct analyses for correlation with genetic diagnosis. In some reports of MRI findings of OPCA, including the Menzel type of OPCA, which probably included SCA2 and SCA1, and the nonhereditary Dejerine–Thomas type of OPCA, degeneration and deciduation of neurons in the inferior olivary nucleus, pontine nuclei, and cerebellum are thought to be characteristic of OPCA, and the MRI findings reflect these characteristics. In one such report, MRI showed atrophy in the pontine base, cerebellum, and middle cerebellar peduncle, with characteristic signals in the pons that showed degeneration of the pontine transverse fiber as well as abnormal signals of the middle cerebellar peduncle and cerebellar white matter (21). The superior cerebellar peduncle was well preserved, however. These imaging findings clearly differ from those of MJD and DRPLA (22,23), which are autosomal dominant spinocerebellar degenerations that show their main pathologic changes in the dentatorubral system and pallidosubthalamic system. There are some reports useful for differentiating these conditions from OPCA as well as for coping with and understanding the pathologic findings (22,23). Both MJD and DRPLA are autosomal dominant spinocerebellar degenerations in which the main pathologic changes occur in the dentatorubral system and pallidosubthalamic system. These diseases occasionally develop similar neurologic symptoms. Degeneration of the globus pallidus is stronger in the inner segment in MJD, whereas degeneration is greater in the outer segment in DRPLA. It is difficult, however, to distinguish these regions sufficiently clearly so as to provide information useful for differentiation by imaging. Magnetic resonance imaging of DRPLA reveals marked midbrain atrophy and atrophy of the pontine tegmentum and basal region, marked atrophy of the cerebellar vermis, and superior cerebellar peduncular atrophy. Abnormal signals dependent on the disease stage or the extent of the CAG repeat were reported in the thalamus, brainstem, and cerebral white matter (23). Abnormal signals detected in the thalamus, brainstem, and cerebral white matter in DRPLA may be findings useful for differentiating this disease from MJD. Based on the present investigation together with previously reported cases, the progression of cerebellar atrophy is slight compared with the progression of atrophy in the brainstem in MJD, which may also be a finding useful for differentiating MJD from DRPLA. In some patients with short disease duration and in others with slight CAG repeat extension, clinical and

imaging differentiation of MJD and DRPLA is difficult; thus, further investigation is necessary.

Acknowledgment: The authors thank Jun Gotoh of the Department of Neurology at Tokyo University for genetic analysis.

REFERENCES

1. Nakano KK, Dawson DM, Spence A. Machado disease: a hereditary ataxia in Portuguese immigrants to Massachusetts. *Neurology* 1972;22:49–55.
2. Coutinho P, Andrade C. Autosomal dominant system degeneration in Portuguese families of the Azores Islands. *Neurology* 1978;28: 703–9.
3. Sasaki T, Ohta M, Ishino H. Joseph disease in a non-Portuguese family. *Neurology* 1983;33:74–80.
4. Lima L, Coutinho P. Clinical criteria for diagnosis of Machado–Joseph disease: report of a non-Azorean Portuguese family. *Neurology* 1980;30:319–22.
5. Sachdev HS, Forno LS, Kane CA. Joseph disease: a multisystem degenerative disorder of the nervous system. *Neurology* 1982;32: 192–5.
6. Yuasa T, Miyatake T, Ohama E, et al. A comparative study of Machado–Joseph disease in Portuguese and Japanese [in Japanese, English abstract]. *Shinkei Kenkyu No Shinpo [Advances in Neurologic Sciences]* 1990;34:102–12.
7. Inoue Y, Yuasa T. Dentatorubral-pallidoluisian atrophy and Machado–Joseph disease [in Japanese, English abstract]. *Shinkei Kenkyu No Shinpo (Advances in Neurologic Sciences)* 1995;39: 519–28.
8. Takiyama Y, Nishizawa M, Tanaka H, et al. The gene for Machado–Joseph disease tightly linked to the DNA markers on chromosome 14q. *Nat Genet* 1993;4:300–4.
9. Maruyama H, Nakamura S, Matsuyama Z, et al. Molecular features of the CAG repeats and clinical manifestations of Machado–Joseph disease. *Hum Mol Genet* 1995;4:807–12.
10. Murata Y, Yamaguchi S, Kawakami H, et al. Characteristic magnetic resonance imaging findings in Machado–Joseph disease. *Arch Neurol* 1998;55:33–7.
11. Onodera O, Idezuka J, Igarashi S, et al. Progressive atrophy of cerebellum and brainstem as a function of age and the size of the expanded CAG repeats in the MJD1 gene in Machado–Joseph disease. *Ann Neurol* 1998;43:288–296.
12. Etchebehere ECSC, Cendes F, Lopes-Cendes I, et al. Brain single-photon emission computed tomography and magnetic resonance imaging in Machado–Joseph disease. *Arch Neurol* 2001;58: 1257–63.
13. Twist EC, Casaubon LK, Ruttledge MH, et al. Machado–Joseph disease (MJD) maps to the same region of chromosome 14 as the spinocerebellar ataxia 3 locus. *J Med Genet* 1995;32:25–31.
14. Haberhausen G, Damian MS, Leweke F, et al. Spinocerebellar ataxia, type 3 (SCA3) is genetically identical to Machado–Joseph disease (MJD). *J Neurol Sci* 1995;132:71–5.
15. Abe Y, Tanaka F, Matsumoto M, et al. CAG repeat number correlates with the rate of brainstem and cerebellar atrophy in Machado–Joseph disease. *Neurology* 1998;51:882–4.
16. Orr HT, Chung M, Banfi S. Expansion of an unstable trinucleotide CAG repeat in spinocerebellar ataxia type 1. *Nat Genet* 1993;4: 221–6.
17. Koide R, Ikeuchi T, Onodera O. Unstable expansion of CAG repeat in hereditary dentatorubralpallidoluysian atrophy (DRPLA). *Nat Genet* 1994;6:9–13.
18. Nagafuchi S, Sanagisawa H, Sato K. Dentatorubral and pallidoluysian atrophy: expansion of an unstable CAG trinucleotide on chromosome 12p. *Nat Genet* 1994;6:14–8.
19. Gispert S, Twells R, Orozco G. Chromosomal assignment of the second locus for autosomal dominant cerebellar ataxia (SCA2) to chromosome 12q23–24.1. *Nat Genet* 1993;4:295–9.
20. Yagishita S, Inoue M. Clinicopathology of spinocerebellar degeneration: its correlation to the unstable CAG repeat of the affected gene. *Pathology International* 1997;47:1–15.
21. Savoiardo M, Strada L, Girotti F, et al. Olivopontocerebellar atrophy: MR diagnosis and relationship to multisystem atrophy. *Radiology* 1990;174:693–6.
22. Tomiyasu H, Yoshii F, Ohnuki Y, et al. The brainstem and thalamic lesions in dentatorubral pallidoluysian atrophy: an MRI study. *Neurology* 1998;50:1887–90.
23. Koide R, Onodera O, Ikeuchi T, et al. Atrophy of the cerebellum and brainstem in dentatorubral pallidoluysian atrophy. Influence of CAG repeat size on MRI findings. *Neurology* 1997;49:1605–12.

Journal of Neuropathology and Experimental Neurology
Copyright © 2003 by the American Association of Neuropathologists
Vol. 62, No. 6
June, 2003
pp. 644–654

Accumulation of Phosphorylated α-Synuclein in Aging Human Brain

YUKO SAITO, MD, PHD, AKIKO KAWASHIMA, MSC, NYOKA N. RUBERU, MD, HIDEO FUJIWARA, MSC, SHUNICHI KOYAMA, MD, MOTOJI SAWABE, MD, PHD, TOMIO ARAI, MD, PHD, HIROSHI NAGURA, MD, HIROSHI YAMANOUCHI, MD, PHD, MASATO HASEGAWA, PHD, TAKESHI IWATSUBO, MD, PHD, AND SHIGEO MURAYAMA, MD, PHD

Abstract. α-Synuclein in Lewy bodies (LBs) is phosphorylated at Ser129. We raised monoclonal and polyclonal antibodies to this phosphorylation site (psyn) and examined 157 serial autopsy brains from a geriatric hospital. Anti-psyn immunoreactivity was observed in 40 of these cases (25.5%). Immunohistochemistry revealed 4 novel types of pathology: diffuse neuronal cytoplasmic staining (pre-LB); neuropil thread-like structures (Lewy threads); dot-like structures similar to argyrophilic grains (Lewy dots); and axons in the white matter (Lewy axons). This novel pathology was abundantly present around LBs and also involved the limbic subcortical white matter, the cerebral cortical molecular layer, and the spongiform changes of the medial temporal lobe associated with cases of dementia with LBs (DLB). The phosphorylated α-synuclein was limited to the temporal lobe in cases of Parkinson disease, spread from the temporal lobe to the frontal lobe in cases of DLB transitional form and further spread to the parietal and occipital lobes in DLB neocortical form. Our findings suggest that LB-related pathology initially involves the neuronal perikarya, dendrites, and axons, causes impairment of axonal transport and synaptic transmission, and later leads to the formation of LBs, a hallmark of functional disturbance long before neuronal cell death.

Key Words: α-Synucleinopathy; Axon; Dementia with Lewy bodies; Immunohistochemistry; Parkinson disease; Synapse.

INTRODUCTION

Lewy body (LB)-related pathology was originally recognized in the brains of patients with Parkinson disease. Since it was discovered that ubiquitin (1) and α-synuclein (2, 3) are components of LBs, the locations of LB-related pathology and the corresponding specific neurological abnormalities have received considerable attention. Involved sites include the peripheral autonomic nervous system in cases with autonomic failure (4), the dorsal motor nucleus of the vagus nerve in cases with dysphagia (5), and the limbic system and neocortex in cases with cognitive decline (i.e. dementia with Lewy bodies [DLB]) (6). The severity of clinical abnormalities in these cases parallels the number of LBs (7) rather than neuronal cell loss (8), especially in cases with DLB neocortical form.

Recent immunohistochemical studies with anti-α-synuclein antibodies suggest that the dorsal motor nucleus of the vagus is the initial site of involvement in Parkinson disease (9). In contrast, α-synuclein-positive structures preferentially localize in the amygdala in familial (10) and sporadic (11) Alzheimer disease (AD). Further clarification of the relationship between these 2 reported types of α-synucleinopathy has been difficult, because α-synuclein is a normal constituent of presynaptic structures (12), and interpretation of abnormal accumulations based on staining intensity may be influenced by the conditions of staining or fixation.

We recently reported that the α-synuclein accumulated in LBs (13) is phosphorylated at Ser129, and that a polyclonal anti-phosphorylated α-synuclein antibody (anti-PSer129) produced strong staining of LBs and Lewy neurites (13). We have now raised a monoclonal antibody (psyn#64) that specifically recognizes this phosphorylation site. Immunohistochemistry with this highly specific monoclonal antibody produces intense staining of LBs and Lewy neurites without staining normal presynaptic structures.

In the current study, we examined serial autopsy brains from an aging population to assess the progression of the 2 reported types of LB-related α-synucleinopathy. We also correlated the morphological changes with the severe functional impairment that occurs prior to cell loss in LB-related cognitive decline.

MATERIALS AND METHODS

Tissue Source

One hundred and fifty-seven serial autopsy brains from Tokyo Metropolitan Geriatric Hospital (TMGH) were studied in the present work. The patients' ages ranged from 48 to 100 years. The mean age was 81.1 ± 8.6 years and the male to female ratio was 89:68.

From Department of Neuropathology, Tokyo Metropolitan Institute of Gerontology (YS, NNR, SK, SM), Tokyo, Japan; Department of Neuropathology and Neuroscience, Graduate School of Pharmaceutical Science (AK, HF, TI), University of Tokyo, Tokyo Japan; Department of Neurology, Division of Neuroscience, Graduate School of Medicine (NNR), University of Tokyo, Tokyo, Japan; Department of Geriatric Medicine (SK), Tokyo Medical University, Tokyo, Japan; Departments of Pathology (MS, TA) and Neurology (HN, HY), Tokyo Metropolitan Geriatric Hospital, Tokyo, Japan; Department of Molecular Neurobiology (MH), Tokyo Institute of Psychiatry, Tokyo, Japan.

Correspondence to: Shigeo Murayama, MD, PhD, Department of Neuropathology, Tokyo Metropolitan Institute of Gerontology, 35-2 Sakaecho, Itabashi-ku, Tokyo 173-0015, Japan. E-mail: smurayam@tmig.or.jp

Sources of support: Foundation of Tokyo Metropolitan Institute of Gerontology.

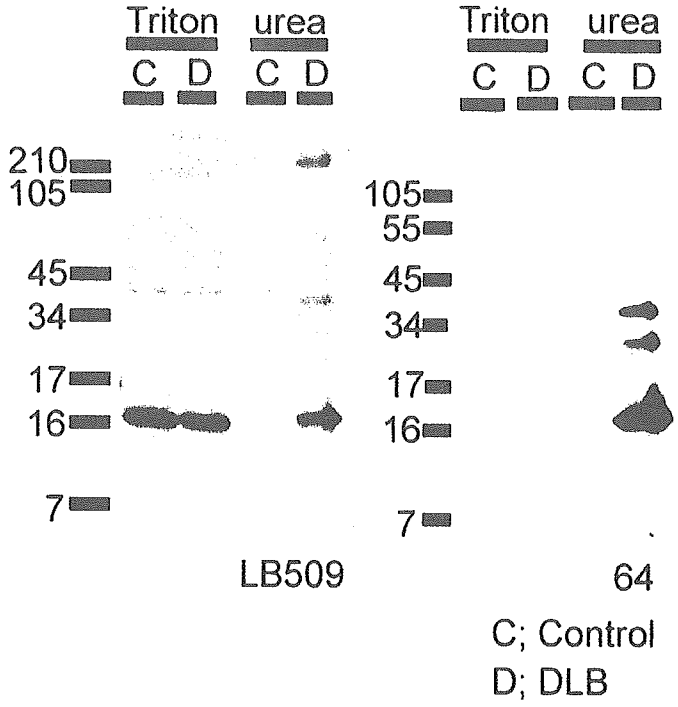

Fig. 1. Western blot analysis of α-synuclein differentially extracted with Triton X-100 (Triton), Sarkosyl, or urea from cerebral cortices of a patient with DLB, neocortical form (Case 4) and a normal control individual probed with LB509 (left panel) or psyn#64 (right panel). Sarkosyl soluble fractions that did not contain detectable amounts of α-synuclein are not shown. Molecular weight markers are shown in kilodaltons at the left side of the panels. A ~15 kDa polypeptide, labeled by LB509 (3), was detected in TX-soluble fractions of DLB and normal control brains and represents normal α-synuclein, as previously reported (13). A major ~15 kDa polypeptide and additional minor higher molecular weight polypeptides were specifically detected by LB509 in Sarkosyl-insoluble, urea-soluble fractions from DLB cortices. Monoclonal antibody psyn#64 did not label TX-soluble α-synuclein, but strongly reacted with the urea-soluble α-synuclein in DLB brains.

Neuropathology

Sections of the right substantia nigra, amygdala, anterior hippocampus and frontal, temporal, parietal, and occipital lobes were fixed in 4% paraformaldehyde for 48 hours and embedded in paraffin. The left half of the brain was fixed in 20% neural buffered formalin (Wako, Osaka, Japan) for 7 to 13 days and representative areas were embedded in paraffin.

Six-μm-thick sections were stained with hematoxylin and eosin (H&E) and by the Klüver-Barrera method. Selected sections were examined with modified methenamine and Gallyas-Braak silver staining for senile changes, with Congo red staining for amyloid deposition, and with elastica Masson staining for vascular changes.

Preparation and Characterization of Anti-Phosphorylated α-Synuclein (psyn) Monoclonal Antibody (psyn#64)

Anti-psyn monoclonal antiobody (psyn#64) was raised against a synthetic peptide corresponding to residues 124–134 of human α-synuclein containing phosphoserine at position 129 and screened by ELISA. For the characterization of the antibody, neocortex from the medial temporal lobe of brains with DLB neocortical form and of normal control brains from the present autopsy series were differentially extracted as previously described (13), with some modifications. Briefly, the neocortices were directly homogenized in 1% Triton X-100 (TX) containing protease inhibitors (instead of Tris saline) and then extracted with Sarkosyl and urea. TX- or urea-soluble fractions, in which normal and deposited α-synuclein is extracted, respectively, were separated by SDS-PAGE and analyzed by immunoblotting with LB509 (3) or psyn#64 as primary antibodies. In addition, the immunoreactivity was confirmed by immunoblot with nonphosphorylated recombinant human α-synuclein and α-synuclein phosphorylated in vitro by casein kinase 2, which specifically phosphorylates Ser129 (3) (A.K., H.F., and T.I., unpublished observation).

Immunohistochemistry

Six-μm-thick serial sections were obtained from paraffin blocks and immunohistochemically stained using a Ventana 20NX autostainer (Ventana, Tucson, AZ) for single or double immunolabeling as previously described (14). Two antibodies specific for phosphorylated α-synuclein (mouse monoclonal antibody psyn#64 and polyconal antibody anti-Pser129 [13]) were used. In addition, other antibodies against α-synuclein (LB509, monoclonal [3] & and S1, recognizing the C terminus [a kind gift from Dr. Y. Ihara]); phosphorylated tau (AT8, monoclonal, Innogenetics, Temse, Belgium); Aβ11-28 (12B2, monoclonal, IBL, Maebashi, Japan); ubiquitin (polyclonal, Sigma-Aldrich, St. Louis, MO); glial fibrillary acidic protein (GFAP, polyclonal, DAKO, Carpinteria, CA); and HLA-DR (CD68, monoclonal, DAKO) were also used. The sections were pretreated with 99% formic acid for 5 min for psyn#64 and anti-Aβ, or heated in a microwave oven (Nisshin EM, Tokyo, Japan) for 10 min in citrate buffer before incubation with LB509, CD68, or anti-ubiquitin antibody. Areas selected for staining with psyn#64 included all of the paraformaldehyde-fixed tissues, as well as areas from the formalin-fixed tissues recommended by the consensus guidelines for dementia with Lewy bodies (DLB) (6) (lumbar, thoracic, and cervical spinal cord, medulla oblongata at the level of the dorsal motor nucleus of the vagus nerve, upper pons at the level of the locus ceruleus, midbrain, and basal ganglia, anterior cingulate and entorhinal cortex, amygdala, and second frontal, temporal and supramarginal gyri).

Phosphorylated α-synuclein was detected in dendrites or axons with confocal double immunofluorescence using anti-Pser129 combined with anti-MAP2 (HM2, monoclonal, Sigma, St. Louis, MO) or anti-phosphorylated neurofilament (SMI 31, monoclonal, Sternberger Immunochemicals, Bethesda, MA) antibody. Primary antibodies were visualized with anti-rabbit Alexa 568 Fluor™ and anti-mouse IgG Alexa 488™ (Molecular Probes, Eugene, OR) using a confocal laser microscope (BioRad, Hercules, CA). SMI 31 was diluted up to 1:10,000 in order to avoid possible cross-reaction with phosphorylated tau protein.

Evaluation of Lewy Body-Related Neuropathology

The brains were initially evaluated and their LB scores calculated from sections stained with H&E and anti-ubiquitin immunohistochemistry, as recommended by the consensus guidelines for DLB (6). The presence of LB-related pathology was

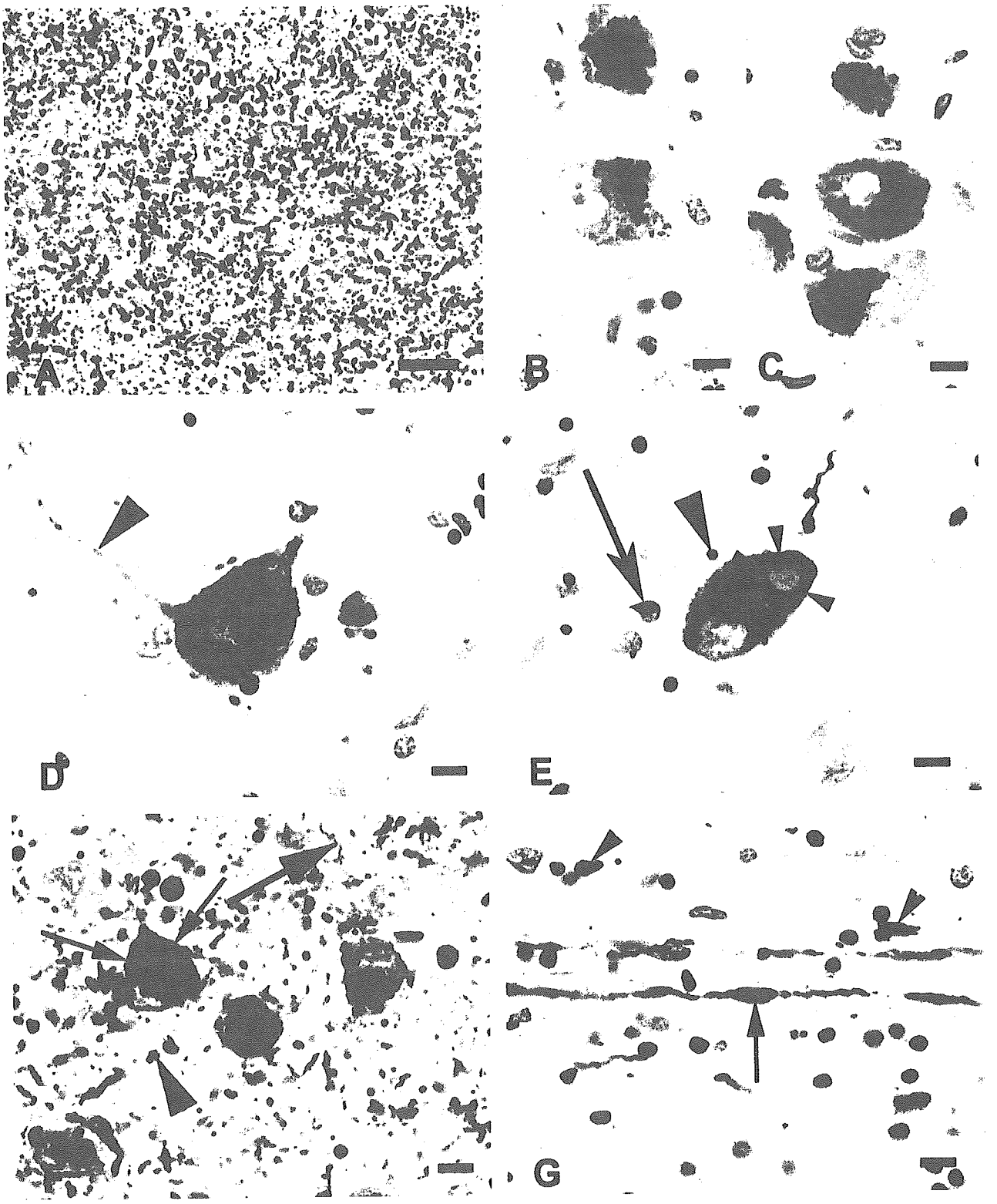

Fig. 2. Novel morphological alterations visualized by immunohistochemistry with anti-phosphorylated α-synuclein (psyn) antibodies. **A:** Numerous dots and threads within the spongiosis in the entorhinal cortex (case 1, bar = 50 μm). **B–E:** Possible morphologic progression in the formation of LBs in melanin-containing neurons of the substantia nigra (Ventana red staining for alkaline phosphatase, bars = 10 μm). **B:** Weak cytoplasmic staining (case 13). **C:** Diffuse cytoplasmic staining (case 14). **D:** Focal cytoplasmic aggregate and positive axon (arrowhead) (case 13). **E:** Typical lamellar staining (small arrowheads), consistent with LBs, associated with neuropil dots (large arrowhead) and a glial inclusion (arrow) (case 6). **F:** Anti-psyn-immunoreactive threads (thick arrow) and dots (arrowhead) with cortical LBs (thin arrows) in the entorhinal cortex (stained with diaminobenzidine) (case 2). **G:** Axons in the white matter of the amygdala (fibrae amygdalofugal) with focal swellings (arrow), positive for anti-psyn antibodies. Anti-psyn-immunoreactive glial inclusions are also visible (arrowheads, case 2).

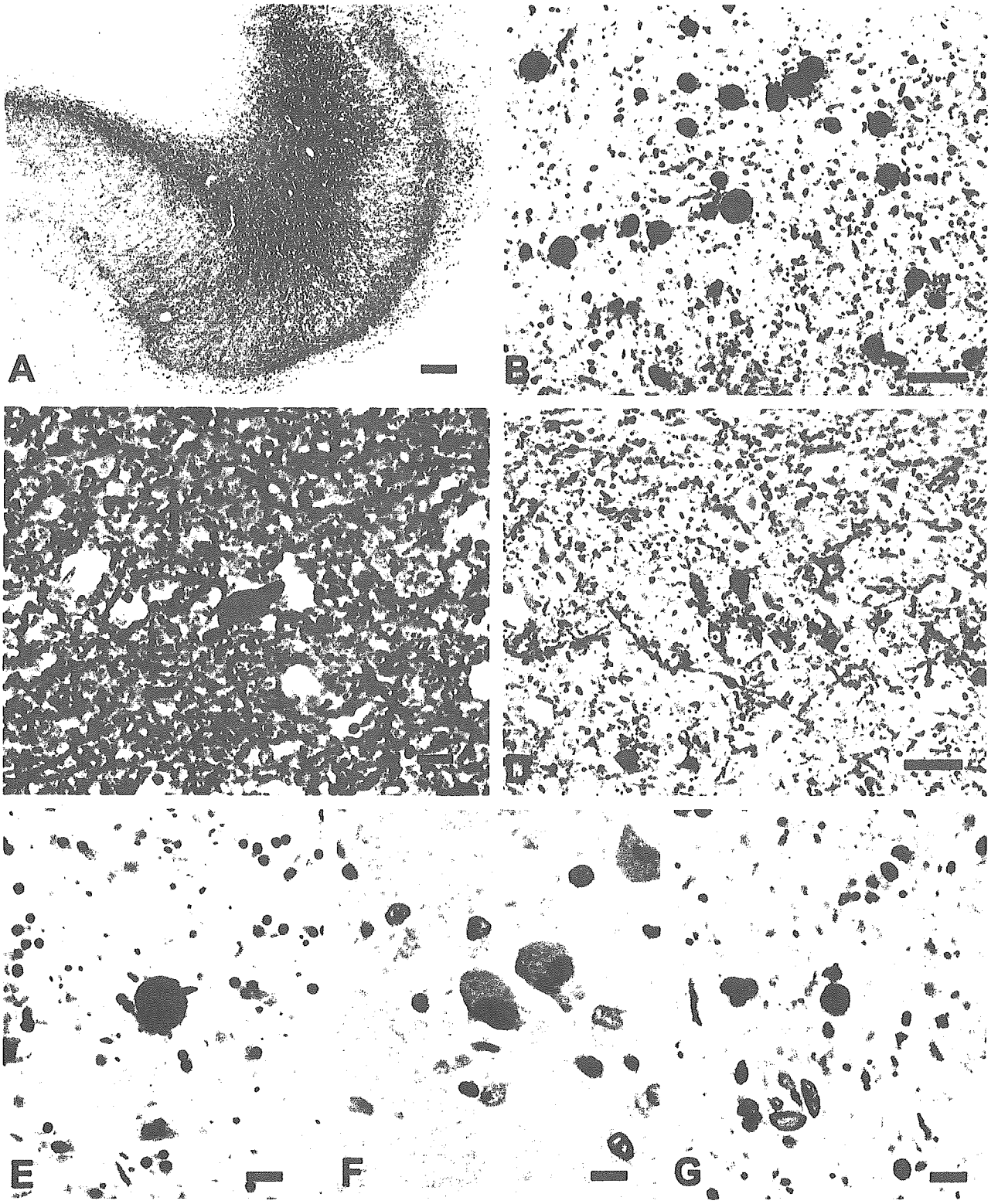

Fig. 3. Morphological alterations visualized by immunohistochemistry with anti-phosphorylated α-synuclein (psyn) antibodies. **A:** Prominent positive staining in the anterior alveus (bar = 0.25 mm, case 2). **B:** Clustered thick neurites in the molecular layer of the anterior subiculum (bar = 50 μm, case 2). **C:** Higher magnification of the alveus shown in (A), showing numerous axons with focal thickening (bar = 10 μm, case 2). **D:** Intracytoplasmic neuronal inclusions with neuritic threads and dots in CA2 and CA3 (bar = 50 μm, case 2). **E:** A large immunoreactive spheroid in the dorsomedial putamen (bar = 10 μm, case1). **F:** Neuronal intracytoplasmic inclusions in the inferior olivary nucleus (bar = 10 μm, case from stage 1B). **G:** Lewy dots, threads, and globules in the molecular layer of the striated cortex (bar = 15 μm, case 1).

immunohistochemically confirmed using anti-α-synuclein antibodies. Sections were then stained for phosphorylated α-synuclein with psyn#64, and based on this staining, a new LB score was calculated using the same criteria referenced above. Selected sections were also stained with polyclonal anti-psyn antibody (13) to confirm the results obtained with monoclonal psyn#64. Small pieces of brain with abundant LB-related pathology were directly fixed in 2.5% glutaraldehyde, postfixed in 1% osmium tetroxide, embedded in epon, and examined in an electron microscope (Hitachi 7500, Hitachi, Japan).

RESULTS

Neuropathology

The 157 serial autopsy brains examined here included 47 cases of neurodegenerative disorders: 15 cases of AD, 13 cases of dementia with grains (DG), 4 cases of DLB neocortical form, 5 cases of DLB transitional form, 2 cases of Parkinson disease, 3 cases of progressive supranuclear palsy (PSP), 1 case of corticobasal degeneration, 1 case of neurofibrillary tangle-predominant form of dementia (NFTD), 1 case of PSP plus DG, 1 case of NFTD plus DG, and 1 case of AD plus DG. All 5 cases with DLB transitional form were categorized as Parkinson disease with dementia, according to McKeith et al (i.e. the onset of dementia was more than 1 year later than the development of parkinsonism) (6, 15). In 3 of the 15 AD cases, LBs were preferentially present in the amygdala; they were abundant in 2 cases and scattered in the third. One case was consistent with LB-related dysphagia (5), with LBs and gliosis preferentially involving the dorsal motor nucleus of the vagus.

Based on examination with H&E staining and immunohistochemistry with anti-ubiquitin antibody, the 157 brains were classified into the following 5 categories: Stage 0: no LBs (128 cases); Stage I: scattered LBs without cell loss (9 cases); Stage II: abundant LBs with macroscopic loss of pigmentation in substantia nigra and locus ceruleus and/or gliosis demonstrated by GFAP immunohistochemistry in the areas containing LBs but without attributable parkinsonism or dementia (9 cases); Stage III: Parkinson disease (2 cases); Stage IV: DLB, transitional form (5 cases); and Stage V: DLB, neocortical form (4 cases).

Characterization of Anti-Phospho-α-Synuclein (psyn) Antibody

Western blotting of the differential extracts from DLB and control brains revealed a ~15 kDa polypeptide that was labeled by a human-specific anti α-synuclein antibody (LB509) (3). The polypeptide was detected in TX-soluble fractions from DLB and normal control brains and represents normal α-synuclein, as previously reported (13) (Fig. 1). A major ~15 kDa polypeptide and a minor additional higher molecular weight polypeptide, which may correspond to ubiquitinated α-synuclein species (16), were detected by LB509 in Sarkosyl-insoluble, urea-soluble fractions from DLB cortices. Monoclonal antibody (mAb) psyn#64 did not label TX-soluble α-synuclein, but strongly reacted with the urea-soluble α-synuclein in DLB brains in an identical pattern to that observed using a phosphorylated Ser129-specific polyclonal antibody, (anti-PSer129) (3). Given that urea-soluble α-synuclein in DLB brains is highly phosphorylated at Ser129 and Tris/TX-soluble normal α-synuclein is not (3), the data are consistent with mAb psyn#64 reacting similarly to anti-PSer129, with the phosphorylation-dependent epitope around PSer129 of α-synuclein. On Western blotting of recombinant human α-synuclein, mAb psyn#64 recognized α-synuclein phosphorylated at Ser129 by casein kinase 2 (data not shown) but did not recognize nonphosphorylated α-synuclein.

Anti-Phospho-α-Synuclein (psyn) Immunopathology

Immunohistochemical staining with anti-α-synuclein (LB509 and S1) antibodies improved both the specificity and the sensitivity for LB-related pathology, as compared to anti-ubiquitin immunohistochemistry, but was seriously complicated by diffuse staining of the background with a synaptic, cytoplasmic, or axonal pattern. The background staining was especially pronounced in paraformaldehyde-fixed sections. Occasional spheroids in the amygdala and zona reticulata of the substantia nigra were also moderately immunoreactive with LB509 and S1.

In contrast, immunostaining with mAb psyn#64 did not produce background staining or anti-α-synuclein-immunoreactive spheroids. The mAb did reveal, however, positively staining Lewy dots (Fig. 2A, E, F) and Lewy threads (Fig. 2A, F) in association with LBs (Fig. 2E, F). These immunopositive dots and threads were best visualized in paraformaldehyde-fixed tissues but could also be detected in buffered-formalin-fixed tissues. Focal enlargement along the course of threads, which corresponded to Lewy neurites in adjacent anti-nonphosphorylated α-synuclein-stained sections, was frequently seen (Fig. 3D). The process of LB formation in pigmented neurons of the substantia nigra appeared to progress from faint (Fig. 2B) or intense (Fig. 2C) diffuse cytoplasmic staining (pre-LB) to single or multiple (Fig. 2D) focal cytoplasmic aggregates (corresponding to pale bodies) to typical positive rings with negative cores (corresponding to brainstem-type LBs) (Fig. 2E). Cortical LBs showed a similar process of progression from focal cytoplasmic accumulations of the epitope to round inclusions (Fig. 2F) with or without central pallor. Immunoreactive glial inclusions were occasionally observed among these neuronal lesions (Fig. 2E, G).

Anti-psyn immunohistochemistry also revealed intense immunoreactivity in the alveus in the subcortical area of the anterior subiculum (Fig. 3A, C), where abundant cortical LBs were present. Additionally, there was staining

in the white matter around the amygdala (Fig. 2G) and in the subcortical white matter of the anterior cingulate gyrus.

With confocal microscopy, anti-psyn immunoreactivity in the white matter was almost exclusively colocalized with the epitope of SMI 31 (Fig. 4A–C). In contrast, Lewy dots and threads in the gray matter were partially colocalized with the epitope of anti-MAP2 (Fig. 4D–F) or SMI 31 (data not shown).

Anti-psyn-immunoreactive structures were observed in 11 of the original Stage 0 cases, preferentially in the dorsal motor nucleus of the vagus and medullary reticular formation in 9 cases and in the amygdala in 2 cases (1 AD case and 1 cognitively normal case with grains (CNG) (14). Five of these 11 cases contained only Lewy dots and threads, but no perikaryal immunoreactivity (4 cases with immunoreactivity in the dorsal motor nucleus of vagus or medullary reticular formation and 1 case of AD with immunoreactivity in the amygdala). We included the 6 cases with perikaryal pre-LBs in a new Stage 1 and categorized the 5 cases with only threads and dots into a new Stage 0.5 (Table 1).

Thirteen of the 15 cases that were newly classified as Stage I with anti-psyn immunohistochemistry had positive staining most prominent in the medulla oblongata. The immunoreactivity was exclusively there in 2 cases, extended to the substantia nigra in 4 cases, and extended to the limbic structure in 7 cases. The remaining 2 cases had AD and showed neuronal intracytoplasmic staining exclusively in the amygdala. Some cases also showed focal aggregates of anti-psyn epitope in the inferior olivary nucleus (Fig. 3F), along with positive dots and threads in the dentate nucleus.

The original Stage II cases were newly subclassified into 2 groups: limbic (IIL, 4 cases), and neocortical variant (IIN, 5 cases), based on the new LB scores calculated with anti-psyn immunohistochemistry. Tables 2A and 2B summarize the cases in the original categories II-V based on examination with H&E and anti-ubiquitin antibody. Two AD cases (Cases 14 and 17 that had preferential involvement of the amygdala were classified into IIL (Case 17) and IIN (Case 14) and showed minor but not negligible positive immunoreactivity in the substantia nigra and dorsal motor nucleus of the vagus. These 2 AD cases contained anti-psyn-immunoreactive neuritic plaques and tangles in the amygdala, entorhinal cortex, and prosubiculum. The colocalization of the epitope of phosphorylated tau and psyn was frequent in the sections immunostained for both psyn#64 and AT8 (data not shown). One case of PSP also had preferential involvement of the amygdala, although anti-psyn-immunoreactivity was detected in all areas showing tauopathy, including the posterior horn of the spinal cord (17). In the amygdala, AT8-immunoreactive threads outnumbered psyn#64-immunoreactive threads and were rarely colocalized together in double-immunostained sections (data not shown). All cases of Stages IIL and IIN showed many LBs and Lewy neurites associated with dots in the transentorhinal area, as well as many Lewy neurites and pre-LBs in CA2 and CA3. Thick neurites, which were strongly immunoreactive with anti-psyn, clustered in the molecular layer of the anterior subiculum,. These thick neurites were most prominent in Stage V cases (Fig. 3B), but they were also seen in 1 of 4 cases of Stage IIL and all cases of Stage IIN. Some of these neurites were identified as intraneuritic LBs in the adjacent H&E-stained sections.

Stage III cases presented with definite limbic pathology involving the transentorhinal area, CA2, CA3, and amygdala. The clustered thick Lewy neurites in the molecular layer of the anterior subiculum were seen in all Stage III cases and were more conspicuous than in the Stage II cases. The involved temporal neocortex had numerous cortical LBs and neurites surrounded by dots and threads. Lesions involving hippocampal CA2 and CA3 were observed in all Stage III cases. The lesions gradually decreased in severity from frontal to parietal cortex, although number of anti-psyn-immunoreactive LBs or intraneuronal aggregates of psyn-immunoreactivity in parietal cortex were still sufficiently numerous for a score of 2, based on the published consensus guidelines (6).

Stage IV cases showed considerable anti-psyn immunoreactive structures in frontal neocortex, including the molecular layer, and in temporal neocortex. There was moderate immunoreactivity in the parietal cortex and mild immunoreactivity in the occipital cortex and striatum. The entorhinal and transentorhinal cortex showed spongiosis associated with numerous Lewy dots and accompanied by psyn-immunoreactive tangles. Approximately 10% of these tangles were also AT8-immunoreactive in double-immunostained sections (data not shown). The lesions in hippocampal CA2 and CA3 were more severe than those in Stage III cases.

Stage V cases showed more widespread neocortical involvement by anti-psyn immunoreactive structures and by degeneration in the limbic system. The lesions in CA2 and CA3 (Fig. 3D) and the spongiosis with numerous Lewy dots in the entorhinal and transentorhinal areas were more conspicuous in Stage V than Stage IV. Psyn-immunoreactive tangles were also more frequent in Stage IV. Scattered neuropil threads, which were immunoreactive for both AT8 and psyn#64, were present in double-immunostained sections (data not shown). The lesions were also more prominent in Stage V than in Stage IV in the cingulate gyrus, insular cortex and entire medial temporal lobe, and frontal and parietal cortex. Numerous Lewy dots were seen in the putamen, with a ventrolateral to dorsomedial gradient (Fig. 3E). Abundant Lewy dots and threads were also detected in the molecular layer of the affected cortical structures,